NANO: Brief Reports and Reviews
Vol. 16, No. 1 (2021) 2150005 (11 pages)

DOI: 10.1142/S1793292021500053

World Scientific
www.worldscientific.com

Graphene-Wrapped FeOOH Nanorods with Enhanced Performance as Lithium-Ion Battery Anode

Meng Sun, Zhipeng Cui, Huanqing Liu, Sijie Li, Qingye Zhang,
Xiaoli Sheng and Yiqian Wang*
College of Physics, Qingdao University,
No. 308 Ningxia Road Qingdao 266071, P. R. China
**yqwang@qdu.edu.cn*

Received 3 September 2020
Accepted 6 November 2020
Published 26 December 2020

FeOOH nanorods (NRs) wrapped by reduced graphene oxide (rGO) were fabricated using a facile solvothermal method. When used as anode materials for lithium-ion batteries (LIBs), the FeOOH NRs/rGO composites show a higher capacity (490 mAh g^{-1} after 100 cycles at a current density of 100 mA g^{-1}) and better rate capability than pure FeOOH NRs. The enhanced electrochemical performance can be ascribed to the hybrid structure of FeOOH and rGO. On one hand, the introduction of rGO can improve electronic conductivity and reduce charge-transfer resistance for electrode materials. On the other hand, the distinctive structure (FeOOH NRs surrounded by flexible rGO) can effectively buffer large volume change during the Li^+ insertion/extraction process. Our work provides a feasible strategy to obtain high-performance LIBs.

Keywords: LIBs; FeOOH NRs; rGO; electrochemical performance.

1. Introduction

The emergence of new energy vehicles and portable electronic products results in a great demand for storage devices with high energy density. Currently, lithium-ion batteries (LIBs) are the main type of energy storage in most applications.[1–4] Particularly, the electrochemical performance of anode materials plays an important role for LIBs. Thus, it is essential to develop the anode materials with high specific capacity, good rate capability and long cycle life. Over the past two decades, transition metal oxides have been considered as potential candidates to replace traditional graphite due to their high capacity, environmental friendliness and low cost.[5–7] Due to easy availability, natural nontoxicity, low cost and high theoretical capacity, iron oxide materials (Fe_2O_3, Fe_3O_4) are regarded as one kind of most promising candidates for the next-generation LIB anode materials.[8,9] Besides, FeOOH has attracted great attention due to its high theoretical capacity (905 mAh g^{-1}), nontoxicity and environmental friendliness.[10] However, similar to other metal oxide materials with a high specific capacity, FeOOH electrode also suffers from serious pulverization problems caused by large volume change, resulting in an inevitable damage of its structure and thus poor capacity retention.[11–13] Such structural collapse and low electrical and ionic migration of FeOOH lead to a rapid capacity fading in long-term cycles. One approach to overcome this drawback is to hybridize FeOOH with other materials which possess large surface areas and good conductivity.

*Corresponding author.

For this purpose, carbon-based materials have attracted intense interest.

Since the discovery of graphene in 2004, it has attracted great research attention because of its large surface area, good conductivity and stable chemical properties.[14–18] Benefiting from these characteristics, graphene has been used widely in energy-storage, such as supercapacitors[19–21] and batteries.[22–24] Especially, graphene has been considered as an ideal conductive material for LIBs. In recent years, metal oxide/graphene composites have exhibited great improvement in electrochemical applications, such as high reversible capacity, long cycle life and good rate performance.[14,25–30] The introduction of graphene can not only enhance the conductivity of the electrode, but also serve as a buffer substrate for the electrode material, which could effectively mitigate the volume expansion and prevent nanomaterials from crushing during the charge/discharge process.[15,31,32] Therefore, combining FeOOH with graphene would be a good strategy for high-performance LIBs.

In this work, FeOOH nanorods (NRs) wrapped by reduced graphene oxide (rGO) were prepared *via* a simple solvothermal method. When used as an anode material for LIBs, the FeOOH NRs/rGO composites exhibit a higher specific capacity and better rate performance than pure FeOOH NRs. The discharge capacity of FeOOH NRs/rGO composite electrode can reach 490 mAh g^{-1}, while pure FeOOH electrode only delivers 120 mAh g^{-1} after 100 cycles at a current density of 100 mA g^{-1}. The enhanced electrochemical performance can be attributed to the fact that the introduction of rGO can alleviate the volume expansion, inhibit the agglomeration of nanorods and improve the conductivity.

2. Experimental Methods

2.1. *Synthesis of FeOOH NRs*

2 mmol $FeCl_3{\cdot}6H_2O$ was dissolved in a mixture of 30 mL deionized water and 30 mL ethanol, and stirred for 10 min. Then, 20 mL NH_4F aqueous solution (0.47 mol·L^{-1}) was added into the above solution to form a homogeneous solution under vigorous stirring. Subsequently, 110 μL ammonia ($NH_3{\cdot}H_2O$) was added into the above mixed solution, and stirred vigorously for 15 min. Finally, the resulting solution was transferred to a 100 mL autoclave and maintained at 180°C for 1 h. After the autoclave was cooled to room temperature, the final precipitates were washed with deionized water for three times and vacuum dried for 6 h to obtain FeOOH NRs.

2.2. *Synthesis of FeOOH NRs/rGO composites*

Graphene oxide (GO) was prepared using natural graphite by a modified Hummers' method.[17] 2 mL GO dispersion (10 mg/mL) was added into 20 mL deionized water, and then subjected to ultrasonic treatment for 1 h. Subsequently, 2 mmol $FeCl_3{\cdot}6H_2O$ was dissolved in a mixed solution containing 30 mL deionized water and 30 mL ethanol, and stirred for 20 min. Afterward, the mixed solution was added into the graphene suspension to form a uniform solution, accompanied by the addition of 110 μL ammonia ($NH_3{\cdot}H_2O$). Then, 0.34 g NH_4F was added to the suspension, and stirred for 10 min. Finally, the resulting solution was transferred to a 100 mL autoclave and maintained at 180°C for 1 h. After the autoclave was cooled to room temperature, the precipitate was washed with deionized water for three times and dried in vacuum for 6 h to obtain FeOOH NRs/rGO composites.

2.3. *Materials characterization*

The crystal structure of the products was characterized by X-ray diffraction (XRD) using a Rigaku SmartLab X-ray diffractometer with Cu-Kα radiation ($\lambda = 1.5406$Å). The morphology of the samples was characterized by field-emission scanning electron microscope (FESEM, Hitachi S-4800) at an acceleration voltage of 15 kV. Bright-field (BF) images and high-resolution transmission electron microscopy (HRTEM) images were obtained on a JEOL JEM2100F transmission electron microscope (TEM) operated at 200 kV. Thermogravimetric analysis (TGA) was conducted on a Netzsch TG 209 apparatus under an air flow from room temperature to 600°C at a heating rate of 10°C/min.

2.4. *Electrochemical measurements*

The CR2025-type coin cells were assembled in a high-purity argon-filled glove box, where the moisture and oxygen concentration are less than

0.1 ppm, using a lithium foil as a counter electrode. The anodes were prepared by mixing the active material (FeOOH NRs and FeOOH NRs/rGO composites), carbon black and polyvinylidene fluoride (PVDF) in a weight ratio of 70:15:15 (wt.%) onto a pure copper foil. N-methylpyrrolidone (NMP) was used as the solvent. The mass loading of the active materials for the cell testing was 0.72 mg cm^{-2}. The electrolyte was composed of 1 M $LiPF_6$ solution of ethylene carbonate (EC)/dimethyl carbonate (DMC)/diethyl carbonate (DEC) (1:1:1 in volume). The electrochemical performance was tested on a LAND CT2001 battery test system in a voltage range from 0.01 V to 3.00 V. Cyclic voltammetry (CV) measurements (over the potential range from 0.01 V to 3.00 V at a scan rate of 0.3 mV s^{-1}). and electrochemical impedance spectroscopy (EIS) tests (at a frequency range from 100 kHz to 0.01 Hz with a disturbance amplitude of 5 mV) were performed on a Metrohm Autolab electrochemical workstation (PGSTAT 302N).

3. Results and Discussion

Figure 1 presents the XRD patterns of FeOOH NRs and FeOOH NRs/rGO composites. Both patterns exhibit diffraction peaks at 26.8°, 34.1°, 35.3°, 39.3°, 46.6° and 56.1°, corresponding to (130), (400), (211), (301), (411) and (251) planes of the tetragonal FeOOH phase (JCPDS no.: 75-1594).[18] In the pattern of FeOOH NRs/rGO composites, a weak peak observed at about 24° could be attributed to the (002) reflections of the graphene sheets.[33] Moreover, FeOOH NRs/rGO composites exhibit broader diffraction peaks than FeOOH NRs, suggesting that FeOOH NRs/rGO composites have smaller particle size[34]

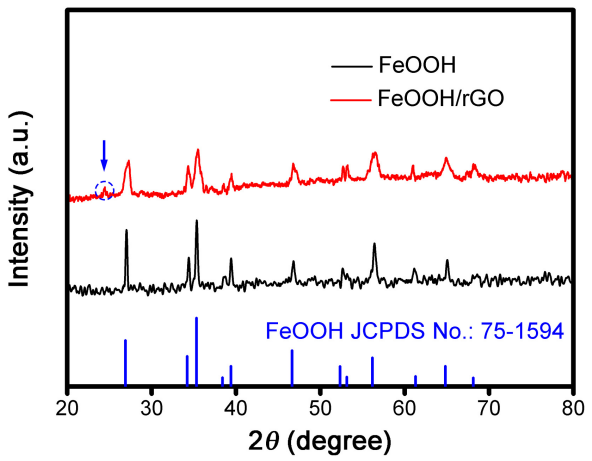

Fig. 1. XRD patterns of the FeOOH NRs and FeOOH NRs/rGO composites.

To investigate the surface morphology and microstructure of FeOOH NRs and FeOOH NRs/rGO composites, extensive SEM and TEM examinations were carried out. Figure 2(a) presents a typical SEM image of pure FeOOH NRs, from which it can be seen that FeOOH NRs are composed of numerous nanoparticles. Figure 2(c) shows a typical SEM image of FeOOH NRs/rGO composites, from which it can be found that the composites consist of fine nanoparticles, and obvious wrinkles are present on their surfaces. These wrinkles result from the stacking of graphene sheets. TEM observations [Fig. 2(b)] of FeOOH NRs indicate that the FeOOH NRs are rod-shaped. The average length and width of FeOOH NRs are measured to be about 35 nm and 10 nm, respectively. TEM observations of FeOOH NRs/rGO composites [Fig. 2(d)] show that FeOOH NRs are wrapped by membrane-like rGO. The introduction of graphene is beneficial to the formation of continuous conductive network. In addition, the rGO sheets can efficiently prevent agglomeration of FeOOH NRs. Such a composite structure can facilitate the electron transport inside the materials, thus leading to the high electronic conductivity.

To study the microstructure of the as-prepared FeOOH NRs/rGO composites in detail, TEM examinations were performed. Figure 3(a) displays a typical BF TEM image of FeOOH NRs/rGO, from which it is observed that FeOOH NRs are surrounded by flexible rGO layer. Figure 3(b) shows a typical HRTEM image of FeOOH NRs/rGO composites, and the lattice spacing is measured to be 2.24 Å, corresponding to (301) crystal plane of FeOOH. TEM examinations suggest that FeOOH NRs/rGO composites are composed of FeOOH NRs and graphene layer. This wrapping design contributes to the formation of continuous conductive networks that promote rapid transport of electrons.

To estimate the content of rGO in FeOOH NRs/rGO composites, TGA measurement was carried out. Figure 4 shows the TGA curves of FeOOH NRs and FeOOH NRs/rGO measured in air from 30°C to 600°C. For the FeOOH NRs, a weight loss is found between 200°C and 430°C, while no weight loss is observed between 430°C and 600°C. The

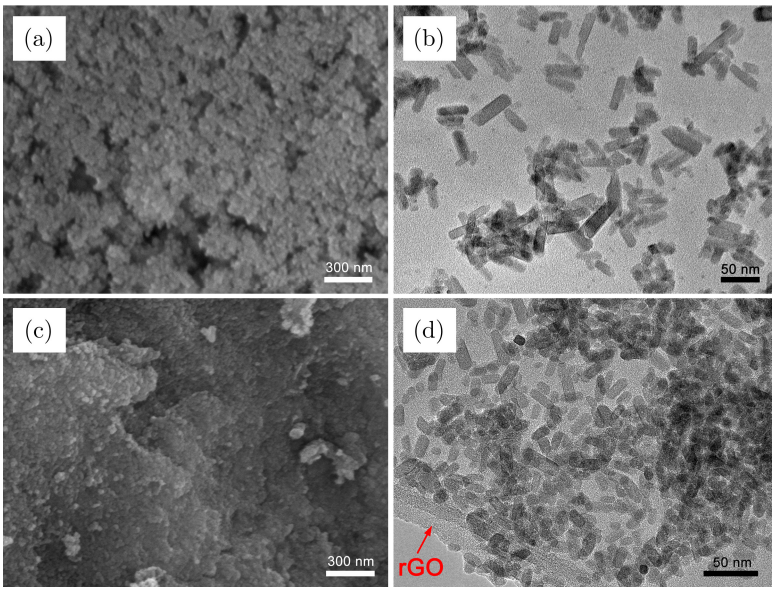

Fig. 2. Typical SEM images of FeOOH NRs (a) and FeOOH NRs/rGO composites (c). Typical BF TEM images of FeOOH NRs (b) and FeOOH NRs/rGO composites (d).

TGA curve of FeOOH has a weight loss of 12.9%, which is close to the theoretical value of FeOOH thermogravimetric loss (10%). For the FeOOH NRs/rGO composites, the small weight loss below 300°C is caused by the thermal decomposition of FeOOH, while the obvious weight loss between 300°C and 500°C results from the oxidation of rGO to CO_2 in air. The whole process shows a total mass loss of 37.5%. The TGA results indicate that the mass proportion of rGO in the composites can be calculated to be about 24.6%.

To explore the lithium storage performance of FeOOH NRs and FeOOH NRs/rGO composites, the assembled half-cells were tested. Figures 5(a) and 5(c) show the first five CV curves of FeOOH NRs and FeOOH NRs/rGO electrodes within a voltage range between 0.01 V and 3.0 V at a scan rate of 0.3 mV s^{-1}, respectively. As observed in Fig. 5(a), in the first cathodic scan, there is a peak near 1.25 V, which corresponds to the formation of intercalated lithium compound by inserting Li^+ into FeOOH.[35] The strong reduction peak near 0.5 V is related to the formation of Fe^0 and a solid electrolyte interphase (SEI) film.[7,11] The oxidation peak at 1.86 V is attributed to the reverse conversion of Fe^0 and Li_2O.[11,34] In the following cycle, the oxidation and reduction peaks move towards a low current, and the area surrounded by CV curves decreases gradually, indicating that the reversibility of FeOOH NRs electrode is poor. In Fig. 5(c), three reduction peaks and two oxidation peaks can be observed in the first scan. The reduction peaks at 2.0 V and 1.25 V correspond to the process of Li^+ intercalation into FeOOH step by step. The reduction peak at 0.44 V corresponds to the formation of Li_2O, Fe^0 and a SEI film.[36,37] In the first anode scan, the peak near 1.2 V

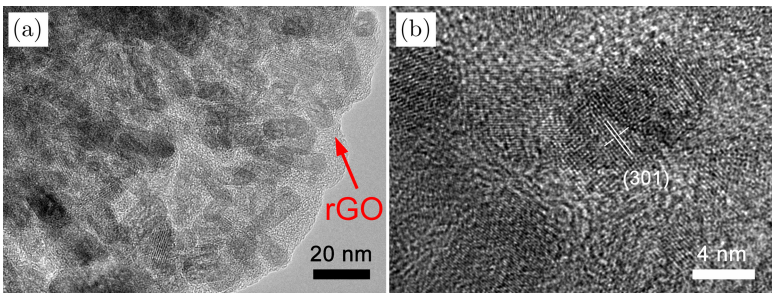

Fig. 3. Typical BF TEM image (a) and HRTEM image (b) of FeOOH NRs/rGO composites.

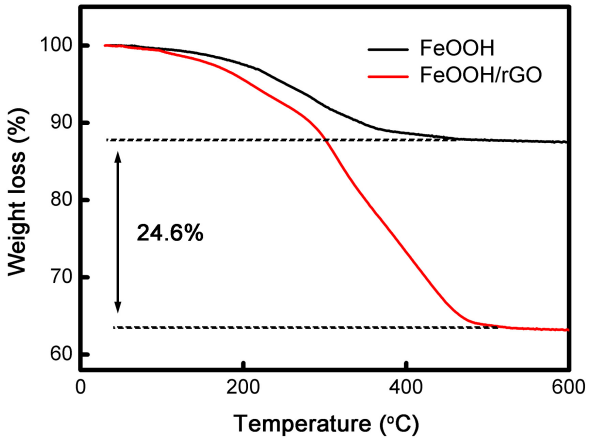

Fig. 4. TGA curves of FeOOH NRs and FeOOH NRs/rGO.

may be caused by the decomposition of SEI film. Another oxidation peak at 1.87 V represents the conversion process of Fe^0 to Li_xFeOOH.[11] In the following cathodic scan, the reduction peaks move to 1.3 V and 0.56 V, slightly higher than those in the first cycle, indicating that the electrode polarization decreases. The CV curves remain unchanged after four cycles, because a stable SEI film has not formed in the FeOOH NRs/rGO composite electrode in the first three cycles.[38] The electrochemical reactions of both anodes during the charge/discharge process can be described by the following equations.[7]

$$\mathrm{FeOOH} + x\mathrm{Li}^+ + x\mathrm{e}^- \leftrightarrow \mathrm{Li}_x\mathrm{FeOOH}, \quad (1)$$

$$\mathrm{Li}_x\mathrm{FeOOH} + \mathrm{Li}^+ + \mathrm{e}^- \leftrightarrow \mathrm{Li}_{1+x}\mathrm{FeOOH}, \quad (2)$$

$$\mathrm{Li}_{1+x}\mathrm{FeOOH} + (2-x)\mathrm{Li}^+ + (2-x)e^- \leftrightarrow \mathrm{Fe}^0 + \mathrm{Li}_2\mathrm{O} + \mathrm{LiOH}. \quad (3)$$

Figures 5(b) and 5(d) display the galvanostatic charge/discharge curves of FeOOH NRs and FeOOH NRs/rGO electrodes after the first, second, fifth and

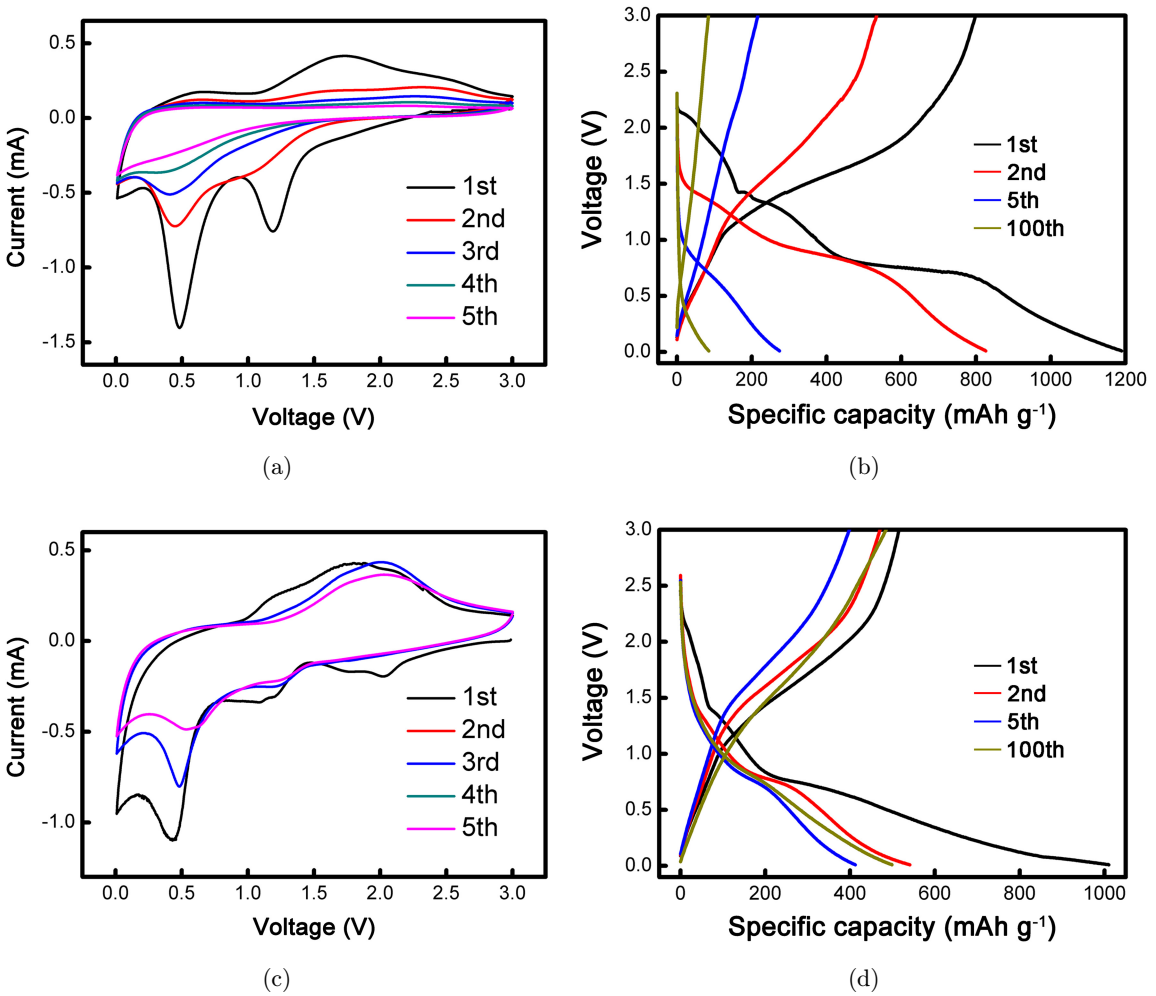

Fig. 5. (a) CV curves at 0.3 mV $s^{-1}$and (b) voltage versus capacity curves at 100 mA g^{-1} of FeOOH NRs. (c) CV curves at 0.3 mV s^{-1} and (d) voltage versus capacity curves at 100 mA g^{-1} of FeOOH NRs/rGO.

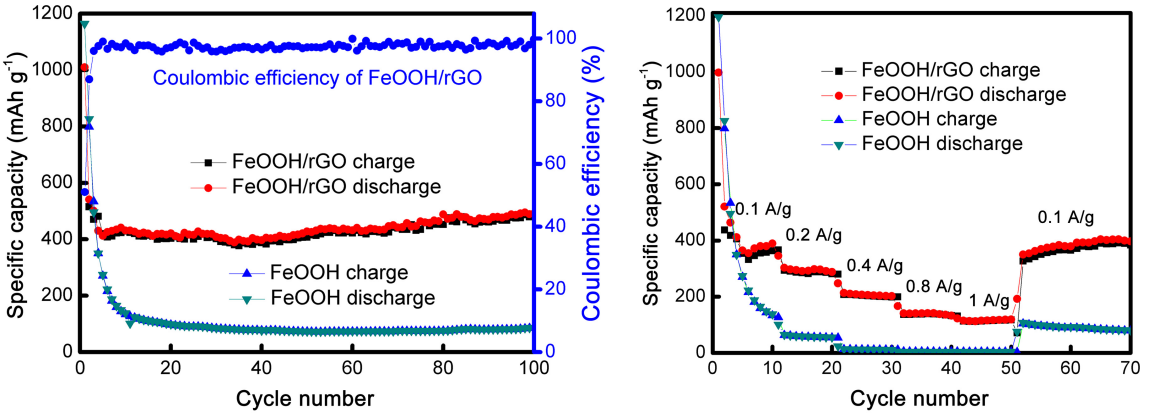

(a) (b)

Fig. 6. (a) Cycling performance at 100 mA g^{-1}, and (b) rate performance at various current densities of FeOOH NRs and FeOOH NRs/rGO electrodes.

100th cycle at a current density of 100 mA g^{-1}, respectively. As shown in Fig. 6(a), the voltage platform of FeOOH electrode becomes shorter with an increase of cycle number. Correspondingly, its specific capacity suddenly drops. At the 100th cycle, the capacity is only 84 mAh g^{-1}, indicating that FeOOH electrode possesses poor reversibility during the electrochemical process. As shown in Fig. 5(d), there are three voltage platforms in the first discharge curve of FeOOH NRs/rGO composite electrode. The platforms at 2.1 V and 1.35 V are attributed to the formation of Li_xFeOOH and $Li_{1+x}FeOOH$ lithium intercalation compounds, respectively. The voltage platform at 0.75 V represents the formation of Fe^0 and a SEI film.[34] In the subsequent discharge curves, three platforms are not obvious, suggesting that the three lithium intercalation reactions are partially irreversible during cycling.[31,39] The first discharge and charge specific capacities of the composites are 1010 mAh $g^{-1}$and 515 mAh g^{-1}, respectively. The irreversible capacity loss can be ascribed to the decomposition of electrolyte and the formation of a SEI film.[32,37]

Figure 6(a) illustrates the cycling performance of FeOOH NRs and FeOOH NRs/rGO electrodes at a current density of 100 mA g^{-1}. FeOOH NRs electrode delivers the first discharge capacity of 1214 mAh $g^{-1}$and its discharge capacity drops to 120 mAh g^{-1} after 100 cycles. It is worth noting that the first discharge capacity of FeOOH NRs/rGO electrode is 1010 mAh g^{-1}, and its discharge capacity maintains around 490 mAh g^{-1}after 100 cycles. Compared to pure FeOOH, FeOOH NRs/rGO electrode delivers a capacity improvement of 370 mAh g^{-1} at a current density of 100 mAg^{-1} after 100 cycles. This is ascribed to the following three points: (i) With the increasing cycles, the electrode material is gradually pulverized, providing more active sites for Li^+ storage. (ii) The rGO sheets increase the conductivity of the electrode. Hence, the charge transfer rate can be increased. (iii) The introduction of flexible rGO can relieve volume expansion during the Li^+ insertion/extraction. Without the rGO coating, the discharge capacity of FeOOH NRs is much lower due to their poor electronic conductivity and severe aggregation upon cycling.

Figure 6(b) shows the rate performance of pure FeOOH and FeOOH NRs/rGO electrodes. The average discharge capacities of FeOOH NRs at current densities of 0.1, 0.2, 0.4, 0.8 and 1 A g^{-1} are 208.4, 125, 81.3, 74.9 and 54.7 mAh g^{-1}, respectively. By contrast, FeOOH NRs/rGO composites deliver an average discharge capacity of 429.2, 328.4, 241.9, 173.1 and 159.2 mAh g^{-1}, respectively. When the current density drops back to 0.1 A g^{-1}, the reversible capacity of FeOOH NRs/rGO composites can be restored to 402.5 mAh g^{-1}, higher than that of FeOOH (156.5 mAh g^{-1}). This implies that the FeOOH NRs/rGO composites exhibit improved rate capability compared to FeOOH NRs electrode during the electrochemical process, in agreement with strong structural stability and conductivity of FeOOH NRs/rGO composites.

To further investigate the capacitive behavior of the FeOOH NRs/rGO electrodes, their reaction kinetics was analyzed by CV measurements, which

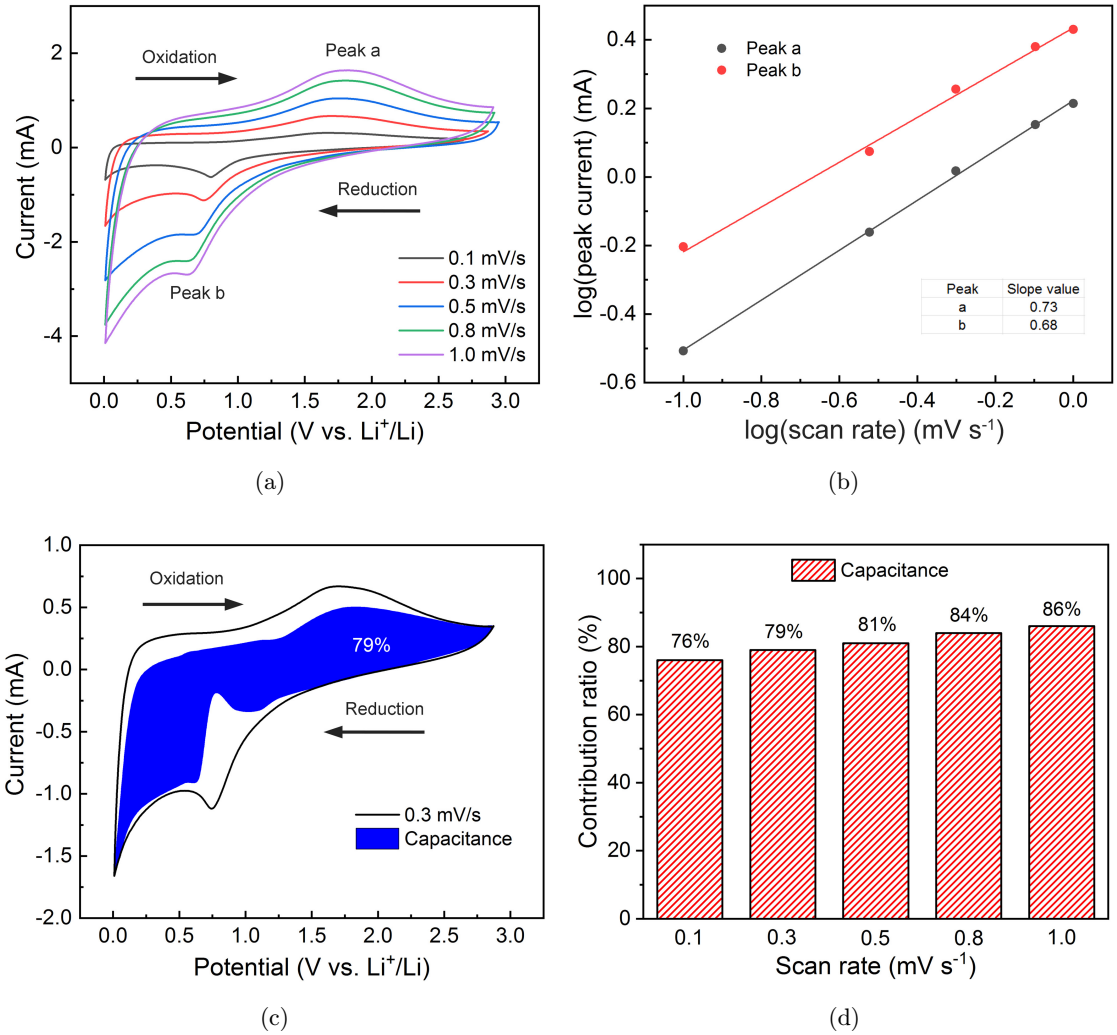

Fig. 7. (a) CV curves of the cell after 30 cycles at different scan rates. b Values of b (slope) at different peak currents after linear fitting. (c) Contribution rate of capacitance at a scan rate of 0.3 mV s^{-1}. (d) Contribution rate of capacitance at different scan rates.

were collected after 30 cycles of the charge/discharge process. As illustrated in Fig. 7(a), the CV curves display similar trends at different scan rates from 0.1 mV $s^{-1}$to 1.0 mV s^{-1}. Normally, the scan rate (v) and the measured current (i) obey the following relationship.[40]

$$i = av^b, \tag{4}$$

where a and b are adjustable parameters. The value of b is determined by the slope of the log$i$ versus log$v$. When the b value is close to 1, the system is mainly controlled by the capacitance process. However, when the b value approaches to 0.5, the diffusion-controlled process dominates the charge transfer. Figure 7(b) shows the b-values at peak currents. The b value is determined to be 0.68 for the reduction process and 0.73 for the oxidation process, which reveals that charge storage partially arises from surface capacitive effect.

To clearly elucidate the capacitance contribution, the total storage of Li^+ can be divided into two parts. The capacitance contribution is calculated according to the following equation.[41]

$$i = k_1 v + k_2 v^{1/2}. \tag{5}$$

$k_1 v$ and $k_2 v^{1/2}$ represent the surface-capacitive effect and diffusion-controlled redox process, respectively. The values of k_1 and k_2 can be obtained by plotting $i(\mathrm{V})/v^{1/2}$ versus $v^{1/2}$, and thus the capacitive current $i_c(\mathrm{V}) = \mathrm{k}_2 v$ could be extracted from the total one. Figure 7(c) shows a typical CV profile for the capacitive current (blue region) compared to the total current. It is observed that 79% of the total Li^+ storage in the electrode is quantified as

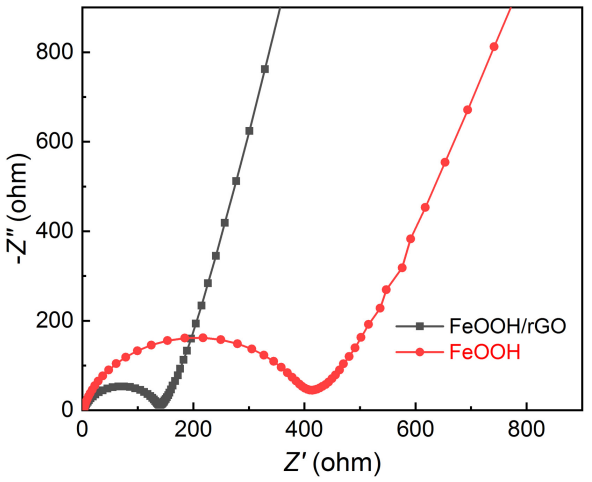

Fig. 8. EIS plots of FeOOH NRs and FeOOH NRs/rGO composite electrodes.

capacitive at the scan rate of 0.3 mV s^{-1}, indicating that most capacity results from the interface of the electrode. The results suggest that the good Li^+ storage performance of FeOOH NRs/rGO electrode can be ascribed to the surface-controlled capacitive behavior. Figure 7(d) illustrates contribution rate of capacitance at different scan rates. It can be found that the contribution rate of capacitance for FeOOH NRs/rGO electrode increases with increasing scan rate.

To further clarify the reasons for the different electrochemical performances between pure FeOOH NRs and FeOOH NRs/rGO composites, EIS measurements were performed. Figure 8 shows the EIS plots of FeOOH NRs and FeOOH NRs/rGO composite electrodes before cycling. It can be clearly seen from Fig. 8 that the EIS spectra consist of a

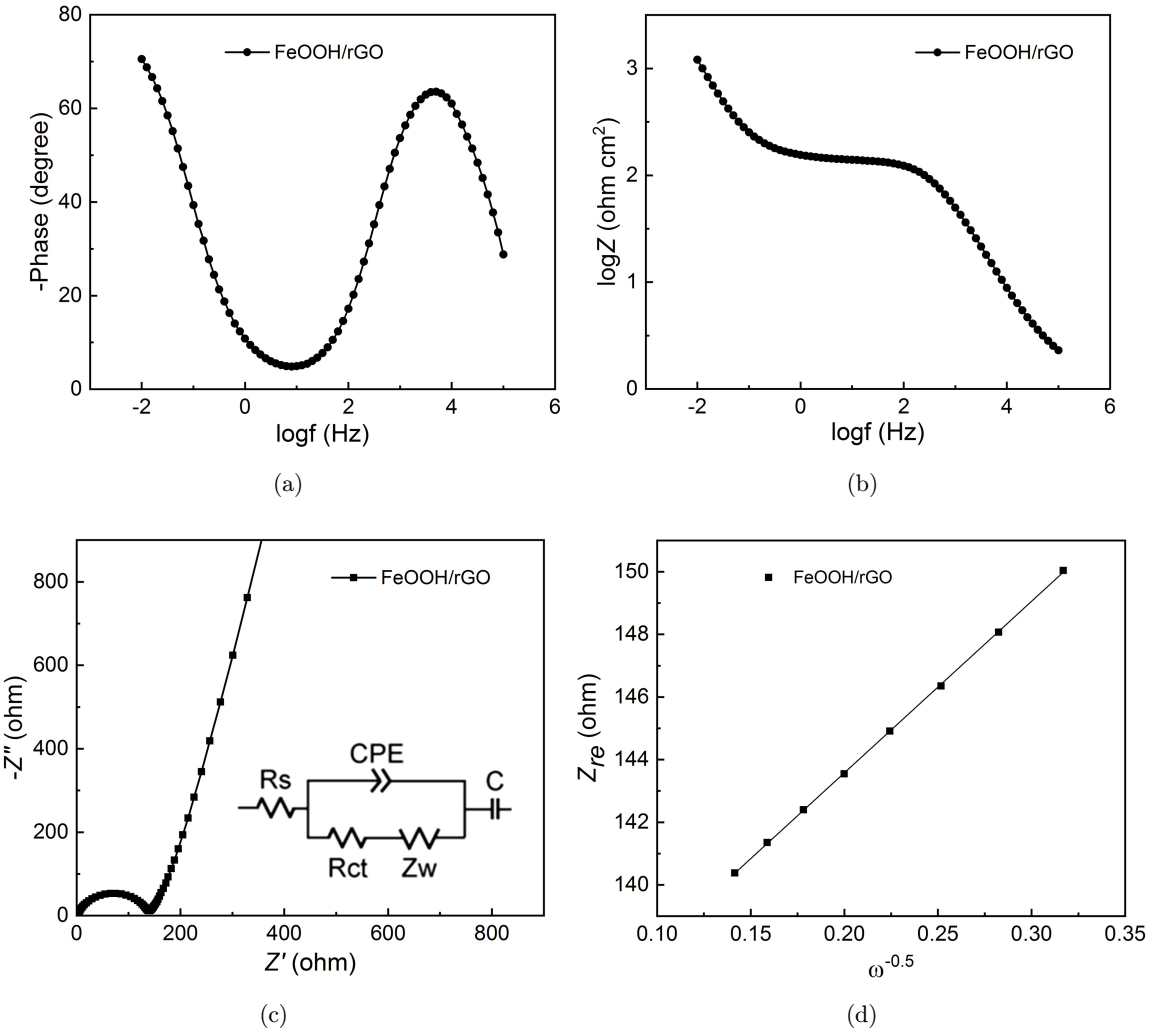

Fig. 9. Bode phase angle diagram (a), and bode magnitude diagram (b) of FeOOH NRs/rGO electrode. (c) EIS of FeOOH NRs/rGO electrode. The inset is the equivalent circuit model. (d) Graph of Z_{re} plotted against $\omega^{-0.5}$.

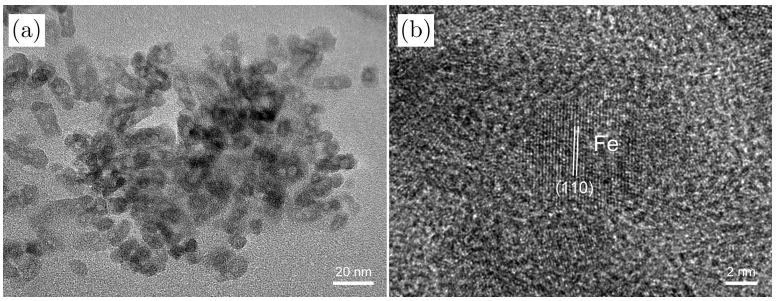

Fig. 10. Typical TEM image (a) and HRTEM image (b) of FeOOH NRs/rGO composite electrode after 100 discharge cycles at a current density of 100 mA g^{-1}.

semi-circle and an inclined line, corresponding to high and low frequency region, respectively. The half-circle diameter of FeOOH NRs/rGO electrode is smaller than that of the FeOOH NRs electrode, implying that FeOOH NRs/rGO electrode has lower contact and charge-transfer resistance.[28,42] Furthermore, in the low-frequency region, the slope of FeOOH NRs/rGO is larger than that of FeOOH, which means FeOOH NRs/rGO electrode possesses better diffusion ability.

EIS measurement was conducted to further understand the electrochemical performance of FeOOH NRs/rGO electrode. From Fig. 9(a), it can be observed that the phase angle is nearly 71° at the low frequency region, which demonstrates a pseudocapacitive feature of the FeOOH NRs/rGO electrode. As shown in Fig. 9(c), the Nyquist plots are composed of a semicircle at high-frequency region and a straight line at low-frequency region. R_s and R_{ct} represent solution resistance and charge transfer resistance, CPE is double-layer capacitance, C is a Faradaic capacitance and Z_w is the Warburg impedance associated with the lithium diffusion. The R_{ct} of FeOOH NRs/rGO electrode is 139 Ω. Furthermore, the inclined line at the low-frequency region indicates that the capacitive-like behavior dominates in the FeOOH NRs/rGO electrode. The diffusion coefficient (D_{Li}) was calculated using the following equations.[41]

$$D_{Li} = \frac{R^2T^2}{2A^2n^4F^4C^2\sigma^2}, \tag{6}$$

$$C = \frac{n}{V} = \frac{m/M}{V}, \tag{7}$$

$$Z_{re} = R_s + R_{ct} + \sigma\omega^{-0.5}, \tag{8}$$

where the constant values of F and R are 96485 C mol^{-1} and 8.314 J K^{-1} mol^{-1}, respectively. A is the electrode area (1.54 $\times 10^{-4}$ m^2), n is the number of the electrons per molecule attending the electronic transfer reaction, T is 298.17 K, and C is calculated to be 1.5 $\times 10^4$ mol m^{-3} from formula (3). Figure 9(d) shows the graph of Z_{re} plotted against $\omega^{-0.5}$. The σ value of FeOOH NRs/rGO electrode is determined to be 54.8 Ω $s^{-0.5}$. The corresponding Li^+ diffusion coefficient of FeOOH NRs/rGO electrode is calculated to be 2.73×10^{-16} cm^2 s^{-1}.

To elucidate the electrochemical process more clearly, a detailed microstructure examination of the FeOOH NRs/rGO electrode (after 100 discharge cycles at 100 mA g^{-1}) was performed. After repeated insertion/extraction of lithium ions, it is still observed that the FeOOH NRs/rGO composites keep a rod-shaped structure [Fig. 10(a)]. TEM observations reveal that the FeOOH NRs/rGO composite structure exhibits superior structural stability, proving that the structure can effectively buffer volume expansion and alleviate strain. Figure 10(b) shows typical HRTEM image of FeOOH NRs/rGO electrode after 100 discharge cycles at 100 mA g^{-1}. The lattice spacing is measured to be 2.03 Å from Fig. 10(b), which corresponds to the lattice spacing of (110) plane of Fe. TEM results suggest that FeOOH is reduced to Fe during the electrochemical process, which is supported by CV curves as shown in Fig. 5(c).

4. Conclusions

In summary, FeOOH NRs/rGO composites were prepared by a facile solvothermal method. The composites are composed of FeOOH nanorods and graphene layer. The average length and width of FeOOH NRs is 36 nm and 10 nm, respectively. When used as an anode material for LIBs, FeOOH NRs/rGO composite electrode exhibits superior lithium storage performance and cycle stability. After 100 cycles at a current density of 100 mA g^{-1},

its reversible specific capacity maintains at 490 mAh g^{-1}, higher than that of pure FeOOH electrode. On one hand, the addition of graphene improves the conductivity of electrode material, and reduces the charge-transfer resistance. On the other hand, the flexible rGO can support FeOOH NRs and relieve large volume change in the process of Li^+ insertion/extraction, which could help to enhance the cycling stability of the electrode. The FeOOH NRs/rGO composite can be considered as a promising candidate for the anode materials of high-performance LIBs.

Acknowledgments

We would like to thank the financial support from the National Natural Science Foundation of China (Grant No. 10974105), Shandong Province "Double-Hundred Talent Plan" Program (Grant No. WST2018006). Y. Q. Wang would also like to thank the financial support from the Taishan Scholar Program, and Qingdao International Center for Semiconductor Photoelectric Nanomaterials and Shandong Provincial University Key Laboratory of Optoelectrical Material Physics and Devices. Meng Sun and Zhipeng Cui contributed equally to this work.

References

1. H. P. Yang, H. H. Wu, M. Y. Ge, L. J. Li, Y. F. Yuan, Q. Yao, J. Chen, L. F. Xia, J. M. Zheng, Z. Y. Chen, J. Duan, K. Kisslinger, X. C. Zeng, W. K. Lee, Q. B. Zhang and J. Lu, *Adv. Funct. Mater.* **29**, 13 (2019).
2. R. P. Fang, K. Chen, L. C. Yin, Z. H. Sun, F. Li and H. M. Cheng, *Adv. Mater.* **31**, 22 (2019).
3. M. Winter, B. Barnett and K. Xu, *Chem. Rev.* **118**, 11433 (2018).
4. Q. S. Wang, L. H. Jiang, Y. Yu and J. H. Sun, *Nano Energy* **55**, 93 (2019).
5. F. J. Lin, M. Yuan, Y. Chen, Y. P. Huang, J. B. Lian, J. X. Qiu, H. Xu, H. M. Li, S. Q. Yuan, Y. Zhao and S. S. Cao, *Electrochim. Acta* **320**, 12 (2019).
6. Y. H. Ding, B. Liu, J. J. Zou, H. Q. Liu, T. Xin, L. H. Xia and Y. Q. Wang, *Mater. Res. Bull.* **106**, 7 (2018).
7. H. Q. Liu, J. J. Zou, Y. H. Ding, B. Liu and Y. Q. Wang, *J. Appl. Electrochem.* **49**, 657 (2019).
8. H. X. Li, Q. Zhou, F. Y. Liu, W. L. Zhang, Z. Tan, H. H. Zhou, Z. Y. Huang, S. Q. Jiao and Y. F. Kuang, *Appl. Catal. B-Environ.* **255**, 9 (2019).
9. Z. H. Chen, Y. Gao, X. Y. Chen, B. L. Xing, C. X. Zhang, S. Wang, T. Liu, Y. Liu and Z. Y. Zhang, *Ionics* **25**, 5779 (2019).
10. Z. H. Chen, Y. Gao, Q. X. Zhang, L. L. Li, P. C. Ma, B. L. Xing, J. L. Cao, G. Sun, H. Bala, C. X. Zhang, Z. Y. Zhang and Y. Y. Zeng, *J. Alloys Compd.* **774**, 873 (2019).
11. M. Imtiaz, Z. X. Chen, C. L. Zhu, H. Pan, I. Zada, Y. Li, S. W. Bokhari, R. Y. Luan, S. Nigar and S. M. Zhu, *Electrochim. Acta* **283**, 401 (2018).
12. H. Qi, L. Y. Cao, J. Y. Li, J. F. Huang, Z. W. Xu, Y. Y. Cheng, X. G. Kong and K. Yanagisawa, *ACS Appl. Mater. Interfaces* **8**, 35253 (2016).
13. X. M. Lou, X. Z. Wu and Y. X. Zhang, *Electrochem. Commun.* **11**, 1696 (2009).
14. D. W. Luo, F. Lin, W. D. Xiao and W. J. Zhu, *Ceram. Int.* **43**, 2051 (2017).
15. S. Bhuvaneswari, P. M. Pratheeksha, S. Anandan, D. Rangappa, R. Gopalan and T. N. Rao, *Phys. Chem. Chem. Phys.* **16**, 5284 (2014).
16. G. H. Qin, H. J. Zhang and C. Y. Wang, *J. Power Sources* **272**, 491 (2014).
17. J. L. Yang, J. J. Wang, D. N. Wang, X. F. Li, D. S. Geng, G. X. Liang, M. Gauthier, R. Y. Li and X. L. Sun, *J. Power Sources* **208**, 340 (2012).
18. K. P. Lopes, L. S. Cavalcante, A. Z. Simoes, J. A. Varela, E. Longo and E. R. Leite, *J. Alloys Compd.* **468**, 327 (2009).
19. S. H. Yang, Y. Li, J. Sun and B. Q. Cao, *J. Power Sources* **431**, 220 (2019).
20. H. Pan, J. Y. Lin, X. Y. Han, Y. Li, X. Meng, R. C. Luo, J. J. Broughton, M. Imtiaz, Z. X. Chen, D. W. Wang, S. M. Zhu, P. Liu and Z. X. Guo, *Nanoscale* **12**, 6562 (2020).
21. S. H. Yang, Y. Y. Liu, Y. F. Hao, X. P. Yang, W. A. Goddard, X. L. Zhang and B. Q. Cao, *Adv. Sci.* **5**, 10 (2018).
22. H. X. Li, M. Xu, C. H. Gao, W. Zhang, Z. A. Zhang, Y. Q. Lai and L. F. Jiao, *Energy Storage Mater.* **26**, 325 (2020).
23. T. Xing, Y. H. Ouyang, L. P. Zheng, X. Y. Wang, H. Liu, M. F. Chen, R. Z. Yu, X. Y. Wang and C. Wu, *J. Energy Chem.* **42**, 108 (2020).
24. Y. Hu, W. Chen, T. Y. Lei, Y. Jiao, H. B. Wang, X. P. Wang, G. F. Rao, X. F. Wang, B. Chen and J. Xiong, *Nano Energy* **68**, 8 (2020).
25. X. Cai, H. B. Lin, X. W. Zheng, X. Q. Chen, P. Xia, X. Y. Luo, X. X. Zhong, X. P. Li and W. S. Li, *Electrochim. Acta* **191**, 767 (2016).
26. Y. Sun, X. H. Liu, F. Z. Huang, S. K. Li, Y. H. Shen and A. J. Xie, *Mater. Res. Bull.* **95**, 321 (2017).

27. Y. Kim, E. Choi, J. G. Kim, S. Lee, W. Yoon, M. H. Ham and W. B. Kim, *ChemElectroChem* **4**, 2045 (2017).
28. C. C. Zhang, Y. H. Xu, W. Y. Chen, L. Y. Sun, D. H. Xu, Y. Yan and X. Y. Yu, *J. Electroanal. Chem.* **816**, 114 (2018).
29. J. G. Kim, Y. Noh, Y. Kim, S. Lee and W. B. Kim, *Nanoscale* **9**, 5119 (2017).
30. Q. M. Su, D. Xie, J. Zhang, G. H. Du and B. S. Xu, *ACS Nano* **7**, 9115 (2013).
31. K. S. Lee, S. Park, W. Lee and Y. S. Yoon, *ACS Appl. Mater. Interfaces* **8**, 2027 (2016).
32. L. Zhou, Z. C. Zhuang, H. H. Zhao, M. T. Lin, D. Y. Zhao and L. Q. Mai, *Adv. Mater.* **29**, 29 (2017).
33. P. Xiong, B. R. Liu, V. Teran, Y. Zhao, L. L. Peng, X. Wang and G. H. Yu, *ACS Nano* **8**, 8610 (2014).
34. K. Q. Zhou, B. A. Wang, J. J. Liu, S. H. Jiang, Y. Q. Shi, Q. J. Zhang, Y. Hu and Z. Gui, *Mater. Res. Bull.* **53**, 272 (2014).
35. Y. J. Zhai, L. Q. Xu and Y. T. Qian, *J. Power Sources* **327**, 423 (2016).
36. T. Tabuchi, Y. Katayama, T. Nukuda and Z. Ogumi, *J. Power Sources* **191**, 636 (2009).
37. L. H. Yu, S. B. Xi, C. Wei, W. Y. Zhang, Y. H. Du, Q. Y. Yan and Z. C. Xu, *Adv. Energy Mater.* **5**, 8 (2015).
38. Y. M. Sun, X. L. Hu, W. Luo, H. H. Xu, C. C. Hu and Y. H. Huang, *ACS Appl. Mater. Interfaces* **5**, 10145 (2013).
39. S. Kakuta, T. Numata and T. Okayama, *Catal. Sci. Technol.* **4**, 164 (2014).
40. D. L. Chao, C. R. Zhu, P. H. Yang, X. H. Xia, J. L. Liu, J. Wang, X. F. Fan, S. V. Savilov, J. Y. Lin, H. J. Fan and Z. X. Shen, *Nat. Commun.* **7**, 8 (2016).
41. A. Y. Shenouda and H. K. Liu, *J. Power Sources* **185**, 1386 (2008).
42. K. Amine, H. Yasuda and M. Yamachi, *J. Power Sources* **81**, 221 (1999).